

Chapter 1

Results and analysis

In this chapter we will showcase a series of results from the MEQSILHOUETTE simulator in order to demonstrate it's capabilities and predictions.

1.1 Canonical simulations

Author's note: This section draws largely from the work of Blecher et al. [2016].

ISM variability and substructure

First we remind the reader of the reproduction of the Ortiz-León et al. [2016] result, shown in Fig. ???. To obtain this result we ran 50 simulated observations, each with an independent realisation of the ISM scattering screen. The success of the reproduction verifies a large section of the simulation software, including I/O, the interferometric and the ISM modules.

Building on the work in the section ???, we will compare the predictions of the ensemble-averaging regime, which consists of only a Gaussian convolution, and the average regime, which includes the presence of stochastic substructure.

“We present the results of a simulated observation of 10 minutes duration at 14:00 UTC on four consecutive days in Fig. 1.1. To compare to published observations, we use the three-station EHT array consisting of the Submillimeter Telescope (SMT) in Arizona, the Combined Array for Research in Millimeter-wave Astronomy (CARMA) in California and the James Clerk Maxwell Telescope (JCMT) on Mauna Kea, Hawaii. The relative transverse velocity between the observer and scattering screen is set to 50 km s^{-1} to be consistent with Ortiz-León et al. [2016]. The source is a circular Gaussian with a $\text{FHWM} = 40 \mu\text{-arcsec}$, approximately the angular distance that a scattering screen would travel over ~ 4 days. The source size has been chosen such that it is consistent with the latest estimate of the size of Sgr A* at 230 GHz [Fish et al., 2011]. Closure quantities are model dependent and calculated as specified in Rogers et al. [1995], where the thermal noise was added based on the system equivalent flux density (SEFD) table in [Lu et al., 2014].

Fig. 1.1 provides an example of closure phase and flux variability over a 4 day period using a static source. Accurate simulation of the ISM-induced closure phase variation is essential in order to make any inference on asymmetric, event-horizon scale structure [e.g. Fish et al., 2016, Ortiz-León et al., 2016]. This will become even more important as the EHT sensitivity increases by an order of magnitude in the near future when phased ALMA is included in the array.” [Blecher et al., 2016]

Note that if the source has intrinsic spatial variability as in the case of a hotspot model Doeleman et al. [2009], this will increase ISM variability as the relative motion between source, screen and observer is increased. Furthermore, ISM scattering simulations can constrain the variability fraction associated with the screen, enabling a more robust estimation of source vari-

ability.

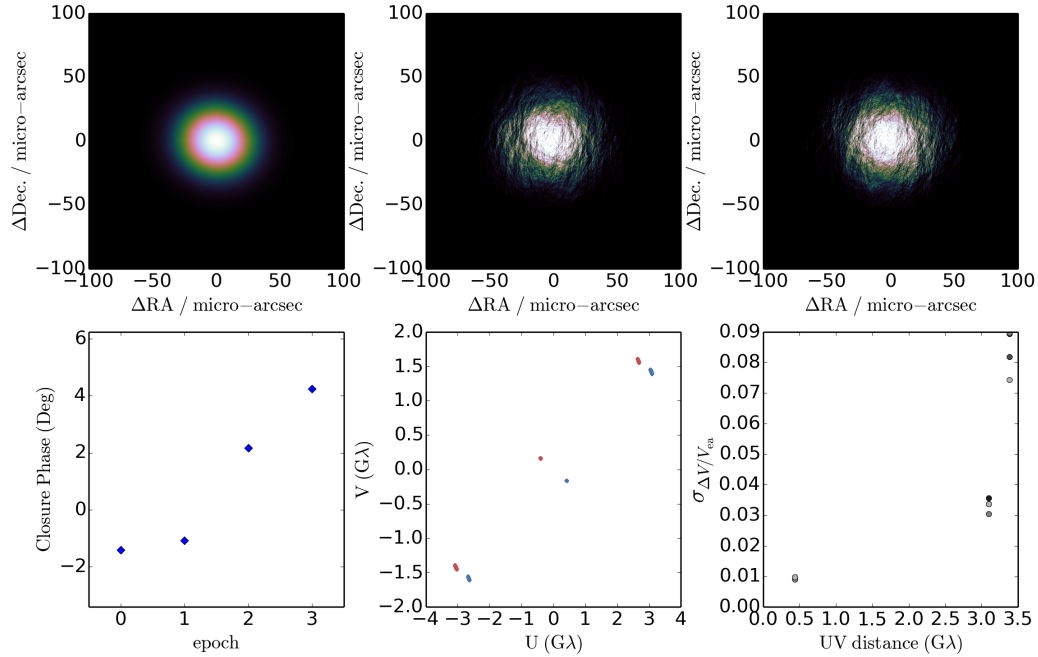


Figure 1.1: “An example simulation of ISM scattering towards Sgr A*, observed with SMT-JCMT-CARMA. The top panel, left to right, shows the original $\text{FWHM} = 40 \mu\text{-arcsec}$ Gaussian (**top left**), the simulated ISM scattered image on the first night (**top middle**) and last night (**top right**) of the observation, respectively. The bottom panel, left to right, shows the evolution of the 10 minute-averaged closure phase with epoch (**bottom left**), uv-tracks for each night (**bottom middle**) and the RMS fractional visibility amplitude differences $\sigma_{\Delta V}/V_{\text{ea}}$ as a function of uv-distance (**bottom right**). $\Delta V = (|V_a| - |V_{\text{ea}}|)$, where $|V_a|$ and $-|V_{\text{ea}}|$ are the simulated average and ensemble average visibility amplitudes respectively. Variations from the ensemble-average flux on the shortest baselines reveal total flux modulation while flux variations on longer baselines and non-zero closure phases track the fluctuations in substructure.” (Image and caption reproduced from Blecher et al. [2016])

Atmospheric transmission and scattering

As laid out in section ??, our tropospheric module is separated into mean and turbulent components with the primary observables being opacity, sky brightness temperature and time delay. The first atmospheric result we present is a plot of typical opacities and sky brightness temperatures for ALMA, the Submillimeter Array (SMA) and the South Pole Telescope (SPT), shown in Fig. 1.2. Note that both the opacity and brightness temperature are proportional to ground pressure and inversely proportional to the ground temperature [Blecher et al., 2016].

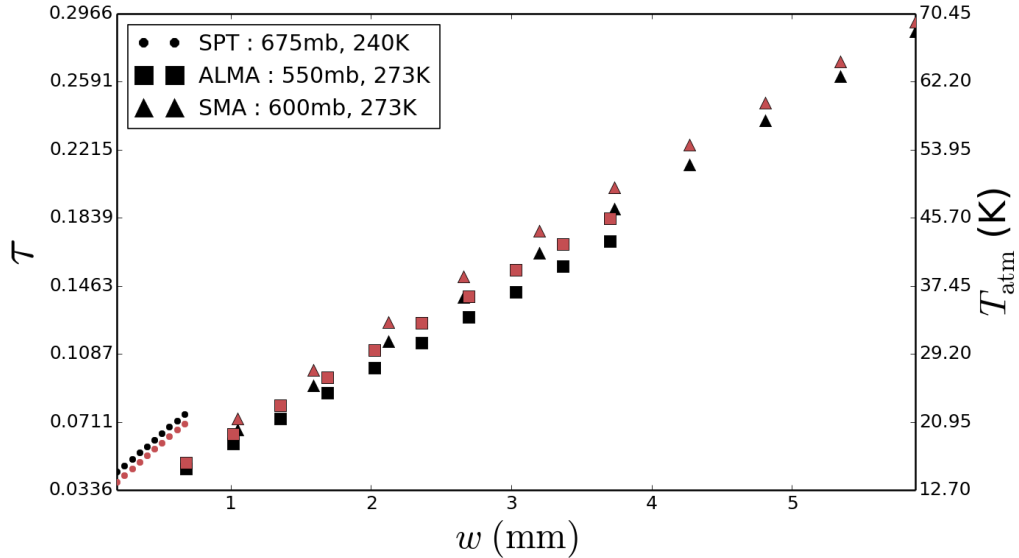


Figure 1.2: “Simulated mean opacity (black) and sky brightness temperature (red) at $\nu = 230$ GHz for three typical ground pressures and temperatures over a typical PWV range [Lane, 1998] which approximately represent the sites of SPT (dots), ALMA (squares) and SMA (triangles). The legend shows the estimated input ground (pressure, temperature) parameters for each site.” (Image and text reproduced from Blecher et al. [2016])

The effects of atmospheric transmission and scattering on delay and delay rate is shown in Fig. 1.3. The total delay is made up of both mean turbulent

components an example of the total and turbulent delays towards Sgr A* is shown for SMA and ALMA.

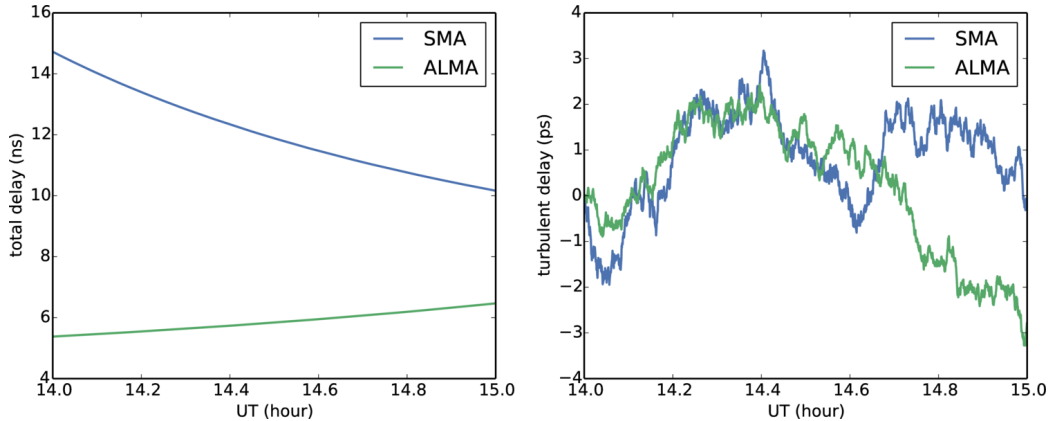


Figure 1.3: “Simulation of the total delay (left) and the turbulent atmospheric delay (right) for SMA (blue) and ALMA (green) sites towards Sgr A*. Ground pressures and temperatures are the same as Fig. 1.2, precipitable water vapour above each station is set to $w = 2$ mm, and the instantaneous zenith coherence time is set $T_0 = 10$ s for both stations. Note that all tropospheric parameters are, however, independently set. The conversion from time delay to phase at 230 GHz is $1 \text{ rad} = 0.7 \text{ ps}$.” (Image and text reproduced from Blecher et al. [2016])

“We now investigate the effect of the tropospheric module on image quality for various levels of calibration accuracy. We simulate the simple scenario of a sky model that consists of a 2.4 Jy point source at the phase centre, which is the approximate EHT-measured flux density of Sgr A* at 230 GHz. We assume a zenith phase coherence time of $t_0 = 10$ s above each station (however, each stations PWV can be independently simulated). We approximate the effect of imperfect calibration by adding a small fraction of the turbulent phase noise. For this example, we do not include the mean delay component, assuming it to be perfectly corrected for during the calibration.” [Blecher et al., 2016]

“In Fig. 1.4 we explore the observational consequences of observing through

a turbulent troposphere. In this simulation, we assume a simple point source model and apply increasing levels of turbulence-induced phase fluctuations before imaging using the two dimensional inverse fast Fourier transforms. We note a rapid attenuation in peak flux due to incoherent averaging, slight offsets in the source centroid and the presence of spurious imaging artefacts. Surprisingly, in this configuration, there was no evidence of blurring or a loss of resolution with the uncertainties. In an upcoming paper, we perform a systematic exploration of the turbulent tropospheric effects on the accuracy of fringe-fitting algorithms/strategies, through use of an automated calibration procedure and including the added complexity of a time-variable source.” [Blecher et al., 2016]

NON-CLOSING ERRORS Non-closing errors due to incoherent averaging - “no conjugates for triples” - possibly comes down to how one defines SNR. In the definition used in the literature we followed, they assumed only gaussian noise, which was not the case..A better definition would be to look at the distribution of a number of samples

Why no seeing? - seeing results when the decoherence is considered as a function of baseline length, longer baseline are more decoherent and their visibilities are downweighted. For the EHT as different stations would experience independent different turbulent intensities, the baseline length will not be correlated with the magnitude of the seeing. But this will still distort the image, leading to uncharacteristic feature extraction....ummm taken the blurring sentence out of the paper on roger’s instruction

Pointing

We investigate the effect of pointing errors on the 50 m (i.e. fully illuminated) Large Millimeter Array (LMT) dish configured in an eight station VLBI array. The LMT has been measured to have an absolute pointing accuracy of $\sigma_{\text{abs}} = 1 - 3$ arcsec, where smaller offsets occur when observing sources closer

to zenith, and a tracking pointing accuracy $\sigma_{\text{track}} < 1 \text{ arcsec}^1$. We investigate the observational effect of these errors through three different pointing error models which explore different instructive and plausible scenarios. The LMT has been singled out as this may well serve as a reference station for the EHT array given its sensitivity and central geographic location. The source used is a circular Gaussian of characteristic size $\Theta_{\text{src}} = 50 \mu\text{-arcsec}$, located at the phase centre. For this investigation, as long as $\Theta_{\text{src}} \ll \theta_{\text{PB}}$, the exact structure of the source is unimportant. We approximate the LMT beam profile using an analytic WSRT beam model [Popping and Braun, 2008] with a factor of two increase in the beam factor C to take into account the increased dish size

$$E(l, m) = \cos^3(C\nu\rho), \quad \rho = \sqrt{\delta l_p^2 + \delta m_p^2} \quad (1.1)$$

where C is a constant, with value $C \approx 130 \text{ GHz}^{-1}$. Note that the power beam EE^H becomes \cos^6 , resulting in a FWHM = 6.5 arcsec at 230 GHz. We make use of the RMS fractional visibility amplitude error $\sigma_{\Delta V/V_0}$, where V_{PE} and V_0 are the visibility amplitudes with and without pointing errors respectively, and $\Delta V = V_{\text{PE}} - V_0$. In Fig. 1.5, $\sigma_{\Delta V/V_0}$ is plotted against pointing error ρ over the range $0 \leq \rho \leq 4.5 \text{ arcsec}$.

In the first case we assume a *constant* pointing error. This simulation is meant to be instructive as to the typical amplitude error in the simplest possible scenario.

In this simulation, we only consider LMT pointing errors due to its narrow primary beam and potential to be used as a reference station. However, the capability to simulate independent pointing errors for each station is available. In the case of a phased array, a pointing error simulation could be used to investigate the contribution of the pointing error to a variable phasing efficiency, which can be reasonably approximated by a scalar Jones matrix.

¹<http://www.lmtgtm.org/telescope/telescope-description/>

In section ??, we show how antenna pointing errors of the LMT could introduce fractional RMS amplitude variations $\sigma_{\Delta V/V_0} \leq 0.4$ on the timescale of phase centre switching. This would occur if the calibrator is widely separated from the source, as is often the case in mm-VLBI. In contrast tracking errors are less problematic with $\sigma_{\Delta V/V_0} \leq 0.05$. If the gain error is non-separable from the calibration model used, it could be interpreted as intrinsic variability, substructure and/or increased noise. If unaccounted for, this effect has the potential to limit the dynamic range of mm-VLBI images. Further tests to constrain the pointing uncertainties of EHT stations will lead to more accurate interferometric simulations and hence the overall impact on black hole shadow parameter estimation. Here we demonstrate the capability to incorporate a range of plausible pointing error effects into a full simulation pipeline.

Visibility amplitude errors due to antenna pointing error has been investigated for the 50 m LMT dish operating at 230 GHz. In Fig. 1.5, we show that pointing errors associated with frequent phase centre switching (stochastic variability) could introduce a RMS fractional amplitude error $\sigma_{\Delta V/V_0} \sim 0.1 - 0.4$ for an absolute pointing accuracy $\sigma_{\text{abs}} \sim 1 - 3$ arcsec. In contrast, tracking errors are less problematic with $\sigma_{\Delta V/V_0} \leq 0.05$ for a tracking accuracy $\sigma_{\text{track}} < 1$ arcsec. The case of a constant error pointing model is comparable to that of the ‘slow variability’ case. If the gain error is non-separable from the calibration model used, it could be interpreted as intrinsic variability, substructure and/or increased noise. If unaccounted for, this effect has the potential to limit the dynamic range of mm-VLBI images. Further tests to constrain the pointing uncertainties of EHT stations will lead to more accurate interferometric simulations and hence the overall impact on black hole shadow parameter estimation. Here we demonstrate the capability to incorporate a range of plausible pointing error effects into a full simulation pipeline. For future observations at 345 GHz, these effects will be even more pronounced, given the narrower primary beam.

1.2 Fringe-fitting test

First we fringe fit and image a stationary point source and compare to the result in Fig. 1.4.

-The authors list a couple of observational challenges and claim that pointing errors, as they have implemented in the simulator, are non-negligible instrumental errors. I think there are more “subtle” instrumental effects that need to be taken into account or should be pointed out to give a full story to the reader. Without an estimate of these effects, I am not sure if you can simply ignore them. A related question: does the simulator have a different treatment of instrumental model for single dish and phased array?

True, there are many additional potential sources of error (e.g. clock errors, bandpass, polarisation leakage, phasing errors, quantisation, correlator model etc.). The point of this first paper is to demonstrate the mm-VLBI framework that enables more sophisticated interferometric simulations. As such, we have focused on capabilities not present in other mm-VLBI simulations and represent different Jones Matrix implementations (i.e. the troposphere, ISM and antenna pointing errors). These also represent amongst the most challenging signal corruptions to implement. As we state in the manuscript, the MeqSilhouette framework, rooted in the Measurement Equation formalism, enables any arbitrary error to be incorporated as a Jones Matrix (e.g. correlator model error is a simple scale matrix $[e^{-\phi}, 0, e^{-\phi}, 0]$). Our intention here is to demonstrate some of the key features of MeqSilhouette and its potential for VLBI simulations for systematic studies that will be reported in future papers. At present, we use the same methods as the other mm-VLBI simulators, but we plan to implement the Jones Matrix approach in the future.

-MeqSilhouette is a VLBI simulator in the first place. The central components described in the paper focus mainly on the signal corruption, but without giving details on the visibility generation and sampling. Given the ultra-wide-band VLBI systems for future observations, are there any systematic uncertainties that a simulator primarily designed for low frequency facilities could bring in?

Visibility generation and sampling is performed through the evalua-

tion of the Fourier Transform at every UVW point in the data. This has been added to the text. Ultra-wide bandwidth observations would require sampling at the appropriate frequency and time resolution in order to avoid smearing effects. MeqTrees can generate visibilities at any arbitrary time and frequency resolution and so we do not anticipate this to be a problem, provided the appropriate choices are made to accurately image the processed field-of-view.

p.2, second last para. The previous simulation work used closure phase as a primary observable, which is in principle immune to station-based phase errors. So I think a nearly perfect phase calibration is well justified, although amplitudes may suffer from systematic calibration errors, which the current work do not consider either for most effects. What is the reason to introduce a variable smoothing kernel? Do you mean refractive substructure?

“The increase in sensitivity and number of EHT stations for the observing run in 2017 marks a shift towards first imaging attempts. Therefore, while previous simulations may have been justified in perfect phase calibration due to a closure quantity only analysis, we now need to move towards a more complex framework to incorporate the relevant corruptions for imaging. Yes, up until now we have considered only several amplitude systematics (pointing error, phase incoherence due to tropospheric turbulence, non-zero atmospheric opacity and emission) but this can be expanded upon in future (specifically a paper on fringe-fitting accuracy and systematics for a range of tropospheric conditions). Yes we mean refractive substructure. This has been clarified in the text. ” [they] assume .. only Gaussian convolution to simulate ISM scattering”

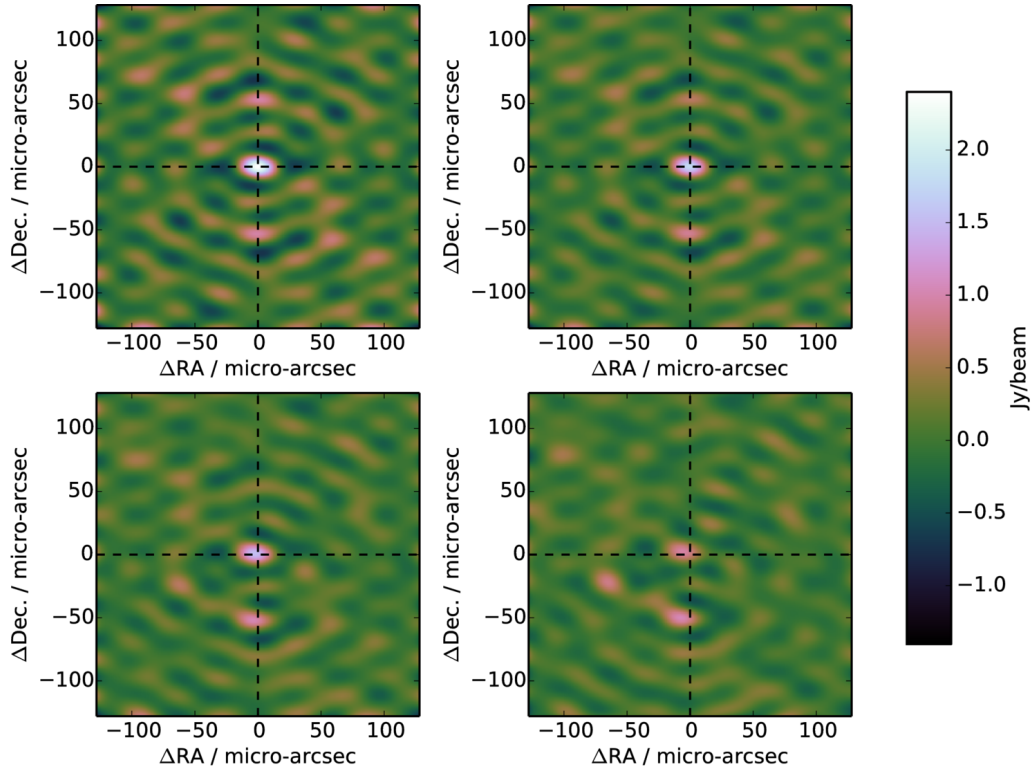


Figure 1.4: “The effect of residual troposphere phase noise on interferometric images of a point source observed for 12 hours at 230 GHz with 4 GHz bandwidth with the following array : SPT, ALMA, SMA, SMT, LMT and JCMT, assuming the same SEFDs as Lu et al. [2014] and an elevation limit of 15° . For simplicity the weather parameters at each station were set to: coherence time $t_0 = 10$ sec; PWV depth $w = 1$ mm; ground pressure $P = 600$ mb; ground temperature $T = 273$ K. **Top left:** interferometric map with thermal noise only. **Top right:** atmospheric attenuation and sky noise (due to non-zero opacity) with 1% of the turbulent phase noise added. **Bottom left:** as previous but with 3% of turbulent phase contribution. **Bottom right:** as previous but with 6% turbulent phase contribution. The fractional turbulent phase contributions are illustrative of the effect of fringe-fitting errors. Note the decrease in the source peak flux with increasing turbulent tropospheric phase noise. Note further that the peak source centroid is offset from its true position (black crosshairs).” (Image and text reproduced from Blecher et al. [2016])

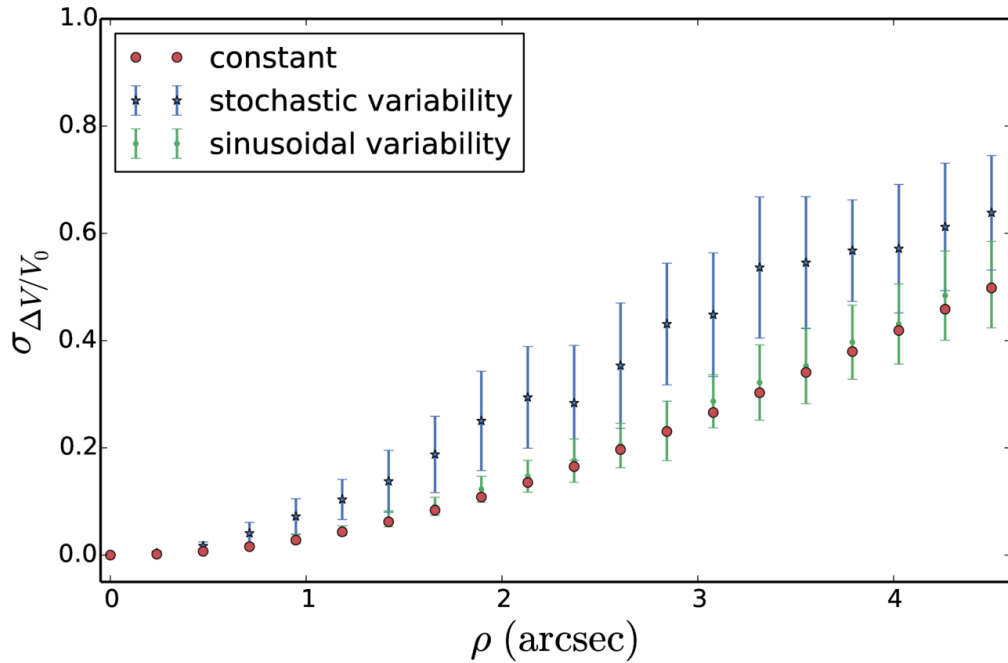


Figure 1.5: “RMS relative amplitude error induced by pointing error with the 50 m (i.e. fully illuminated) LMT antenna as a function of pointing error offset ρ at 230 GHz. We assume that these errors are degenerate or non-separable from the self-calibration/fringe-fitting model used. See text for the description of the three models used. This simulation capability enables constraints on the magnitude of pointing-induced errors given a particular pointing calibration strategy.” (Image and text reproduced from Blecher et al. [2016])

Bibliography

- T. Blecher, R. Deane, G. Bernardi, and O. Smirnov. MeqSilhouette : A mm-VLBI observation and signal corruption simulator. *MNRAS*, September 2016. doi: 10.1093/mnras/stw2311.
- S. S. Doeleman, V. L. Fish, A. E. Broderick, A. Loeb, and A. E. E. Rogers. Detecting Flaring Structures in Sagittarius A* with High-Frequency VLBI. *ApJ*, 695:59–74, April 2009. doi: 10.1088/0004-637X/695/1/59.
- V. L. Fish, S. S. Doeleman, C. Beaudoin, R. Blundell, D. E. Bolin, G. C. Bower, R. Chamberlin, R. Freund, P. Friberg, M. A. Gurwell, M. Honma, M. Inoue, T. P. Krichbaum, J. Lamb, D. P. Marrone, J. M. Moran, T. Oyama, R. Plambeck, R. Primiani, A. E. E. Rogers, D. L. Smythe, J. SooHoo, P. Strittmatter, R. P. J. Tilanus, M. Titus, J. Weintraub, M. Wright, D. Woody, K. H. Young, and L. M. Ziurys. 1.3 mm Wavelength VLBI of Sagittarius A*: Detection of Time-variable Emission on Event Horizon Scales. *ApJ*, 727:L36, February 2011. doi: 10.1088/2041-8205/727/2/L36.
- Vincent L. Fish, Michael D. Johnson, Sheperd S. Doeleman, Avery E. Broderick, Dimitrios Psaltis, Ru-Sen Lu, Kazunori Akiyama, Walter Alef, Juan Carlos Algaba, Keiichi Asada, Christopher Beaudoin, Alessandra Bertarini, Lindy Blackburn, Ray Blundell, Geoffrey C. Bower, Christiaan Brinkerink, Roger Cappallo, Andrew A. Chael, Richard Chamberlin, Chi-Kwan Chan, Geoffrey B. Crew, Jason Dexter, Matt Dexter, Ser-

- gio A. Dzib, Heino Falcke, Robert Freund, Per Friberg, Christopher H. Greer, Mark A. Gurwell, Paul T. P. Ho, Mareki Honma, Makoto Inoue, Tim Johannsen, Junhan Kim, Thomas P. Krichbaum, James Lamb, Jonathan León-Tavares, Abraham Loeb, Laurent Loinard, David MacMahon, Daniel P. Marrone, James M. Moran, Monika Mościbrodzka, Gisela N. Ortiz-León, Tomoaki Oyama, Feryal Özel, Richard L. Plambeck, Nicolas Pradel, Rurik A. Primiani, Alan E. E. Rogers, Katherine Rosenfeld, Helge Rottmann, Alan L. Roy, Chester Ruszczyk, Daniel L. Smythe, Jason SooHoo, Justin Spilker, Jordan Stone, Peter Strittmatter, Remo P. J. Tilanus, Michael Titus, Laura Vertatschitsch, Jan Wagner, John F. C. Wardle, Jonathan Weintraub, David Woody, Melvyn Wright, Paul Yamaguchi, André Young, Ken H. Young, J. Anton Zensus, and Lucy M. Ziurys. PERSISTENT ASYMMETRIC STRUCTURE OF SAGITTARIUS A* ON EVENT HORIZON SCALES. *ApJ*, 820(2):90, mar 2016. doi: 10.3847/0004-637x/820/2/90. URL <http://dx.doi.org/10.3847/0004-637x/820/2/90>.
- A. P. Lane. Submillimeter Transmission at South Pole. In G. Novak and R. Landsberg, editors, *Astrophysics From Antarctica*, volume 141 of *Astronomical Society of the Pacific Conference Series*, pages 289–295, 1998.
- Ru-Sen Lu, Avery E. Broderick, Fabien Baron, John D. Monnier, Vincent L. Fish, Sheperd S. Doeleman, and Victor Pankratius. IMAGING THE SUPERMASSIVE BLACK HOLE SHADOW AND JET BASE OF M87 WITH THE EVENT HORIZON TELESCOPE. *ApJ*, 788(2):120, may 2014. doi: 10.1088/0004-637x/788/2/120. URL <http://dx.doi.org/10.1088/0004-637x/788/2/120>.
- G. N. Ortiz-León, M. D. Johnson, S. S. Doeleman, L. Blackburn, V. L. Fish, L. Loinard, M. J. Reid, E. Castillo, A. A. Chael, A. Hernández-Gómez, D. H. Hughes, J. León-Tavares, R.-S. Lu, A. Montaña, G. Narayanan, K. Rosenfeld, D. Sánchez, F. P. Schloerb, Z.-q. Shen, H. Shiokawa,

- J. SooHoo, and L. Vertatschitsch. The Intrinsic Shape of Sagittarius A* at 3.5 mm Wavelength. *ApJ*, 824:40, June 2016. doi: 10.3847/0004-637X/824/1/40.
- A. Popping and R. Braun. The standing wave phenomenon in radio telescopes. *A&A*, 479(3):903–913, mar 2008. doi: 10.1051/0004-6361:20079122. URL <http://dx.doi.org/10.1051/0004-6361:20079122>.
- Alan E. E. Rogers, Sheperd S. Doeleman, and James M. Moran. Fringe detection methods for very long baseline arrays. *AJ*, 109:1391, mar 1995. doi: 10.1086/117371. URL <http://dx.doi.org/10.1086/117371>.